Geomech. Geophys. Geo-energ. Geo-resour. (2023) 9:49
https://doi.org/10.1007/s40948-023-00583-7

RESEARCH

Nonlinear flow and permeability anisotropy characteristics in hydraulic fracturing-induced rock fractures subjected to various normal compressive stresses

Junchao Chen · Zhenglu Che · Xiaopeng Su · Lei Zhou · Xiaofei Liu · Liang Zhang

Received: 30 December 2022 / Accepted: 18 April 2023

Abstract Well productivity after hydraulic fracturing is strongly affected by the flow behaviors in created fracture complexity. In this study, gas flow tests were conducted in splitting fractures (induced by Brazilian splitting) and hydraulic fractures (created by hydraulic fracturing) to study the nonlinear fluid flow behaviors in rough fractures. 3D fracture surfaces were first digitally reproduced with a scanner and then the fracture geometry parameters (roughness profile index R_p, the root mean square of the fracture profile wall slope Z_2), aperture distributions were computed for both fractures. The influence of the fracture geometry characteristics on the nonlinear flow behaviors were systematically analyzed. The permeability anisotropy was numerically examined in detail. The results show that R_p, Z_2 and mean aperture of hydraulic fractures are relatively smaller, indicating that the fracture surfaces are smoother. The transmissivity of splitting fracture is relatively higher than that of hydraulic ones, and the ratio of splitting to hydraulic one varies from 2.51 at $\sigma_c = 1$ MPa to 60.95 at $\sigma_c = 40$ MPa. By contrast, splitting fractures have larger critical Reynolds number and lower critical pressure gradient, implying that nonlinearity is easier to occur in splitting fractures. The average Forchheimer coefficient for splitting fractures is 0.00577, which is 1.5 times larger than that (0.0041) for hydraulic ones. In addition, the fractures exhibit strong permeability anisotropy and this anisotropic effect is significantly dependent on the loading stress. In general, the permeability anisotropy in hydraulic fracture is more significant, showing that their permeability anisotropy ratios K are larger and more sensitive to the loading. The obtained results confirm that there exist some discrepancies in flow behaviors between splitting and hydraulic fractures and for more accurate evaluation in engineering practice, hydraulic fractures should be fully considered.

J. Chen · Z. Che · L. Zhang
School of Emergency Management, Xihua University, Chengdu 610039, China

X. Su (✉)
School of Civil Engineering, Chongqing Jiaotong University, Chongqing 400074, China
e-mail: suxiaopeng@cqjtu.edu.cn

L. Zhou
State Key Laboratory of Coal Mine Disaster Dynamics and Control, Chongqing University, Chongqing 400044, China

X. Liu
Sichuan Institute of Safety Science and Technology, Chengdu 610000, China

L. Zhang
Emergency Science Research Academy, Chinese Institute of Coal Science, China Coal Technology & Engineering Group Co., Ltd., Beijing 100070, China

Published online: 02 May 2023

Article highlights

- Geometry characteristics of hydraulic fracturing-induced fractures are calculated.
- Nonlinear flow behaviors in hydraulic fracturing-induced fractures subjected to varying normal loading are experimentally analyzed.
- Permeability anisotropy in hydraulic fracturing-induced fractures is numerically examined.

Keywords Nonlinear flow · Fracture · Hydraulic fracturing · Permeability · Anisotropy

1 Introduction

Hydraulic fracturing is commonly used for unconventional resources exploitation, especially in low permeability reservoirs (Pang et al. 2016). Due to the induced complex hydraulic fracture networks, massive fluid flow channels are created and thereby well productivity is largely enhanced. The created complexity is primarily constituted by the fractures with proppant and those without proppant. Apparently, the apertures (the distance between two fracture surfaces) for the fractures with proppant are relatively larger and their change is limited within the exploitation period. Without proppant, fracture apertures are variable and can be easily disturbed by the field stress/mechanical displacement imposed on the fractures. This further complicates the fluid flow behaviors and makes it difficult to accurately describe.

For this reason, flow behaviors through a rough-walled rock fracture subjected to various normal stresses have been extensively investigated for more than a century (Lomize 1951; Witherspoon et al. 1980; Nazridoust et al. 2006; Nemoto et al. 2009; Zhang and Nemcik 2012; McCraw et al. 2016; Kulatilake et al. 2020; Chen et al. 2020; Shen et al. 2020; Dong et al. 2020; Su et al. 2021; Zhu et al. 2022; Ma et al. 2022). Conventionally, linear Darcy's law was widely applied to describe fluid flow behaviors in rock fractures (Brown 2002). Furthermore, based on the assumptions of linear Darcy's law and smooth parallel-plate physical model, the well-known cubic law was proposed (Zou et al. 2015). However, cubic law was proved to be not always convinced to describe the fluid flow characteristics in the real natural fractures (Walsh 1981). Early studies confirmed that cubic law was only limited to low-rate laminar regime whereas nonlinear flow occurs when flow rate becomes adequately large (Qian et al. 2005; Rong et al. 2016). Therefore, nonlinear flow behaviors through rock fractures have been intensively studied by laboratory tests (Zimmerman et al. 2004; Ranjith and Viete 2011) and numerical simulations (Skjetne et al. 1999; Javadi et al. 2010). These studies (Zimmerman and Bodvarsson 1996; Zhou et al. 2015; Zou et al. 2017; Xiong et al. 2018) suggested that fracture geometry was a vital factor that triggers nonlinear flow behaviors. In general, fracture geometry is related to surface roughness, void volume, contact ratio, dilation, matching degree, etc. The change in fracture spatial geometry mainly includes mechanical aperture reduction, asperity deformation and destruction, discrete contact of surfaces and void space isolation. These changes bring about constrictions and obstructions, which are related to aperture distribution and surface roughness of the fracture walls and could strongly affect the fluid flow behaviors through a rock fracture. A point to note is that most of man-made fractures are obtained through Brazilian splitting tests. Strictly, these man-made fractures are not the same as those in engineering practice. It is yet unclear how far the spatial geometries of the fracture induced by hydraulic fracturing deviate from those created through Brazilian splitting. Therefore, there is still a need to compare the surface morphology characteristics of both the mentioned fractures, which further can make it clear how much the discrepancy in surface morphology contributes to nonlinear flow behaviors.

On another aspect, in the process of oil and gas resources exploitation, permeability is an important petrophysical parameter that could largely affect well productivity. With the increase in exploitation depth, the field stress and the sedimentary circumstance are constantly changing, which leads to permeability anisotropy in most reservoirs. To date, most literatures regarding fracture permeability are primarily focused on stress sensitivity and permeability evolution. Only a few studies were carried out to test the fracture permeability anisotropy in a rough rock fracture. Yeo et al. (1998) found that the sandstone fracture permeability becomes larger in the direction perpendicular to the shear displacement than in the direction parallel to the displacement. Méheust and Schmittbuhl (2000, 2001) studied the anisotropic hydraulic

characteristics in a granite fracture and observed that the pressure head orientation strongly controlled the hydraulic response of a single fracture. Watanabe et al. (2008) observed the preferential flow paths in rock fractures even at high confining pressure of 100 MPa. Li et al. (2014) demonstrated that the sandstone fracture exhibited a larger anisotropy in hydraulic conductivities than the shale fracture. Xie et al. (2020) investigated the anisotropic fractal characteristics of sandstone fracture surface and showed that the flow anisotropy of fracture surface was attributed to the various fractal dimension of fracture lines on different directional sections. Shen et al. (2020) found that the coal fracture permeability has strong anisotropy that is primarily caused by the irregular contact shape. It was found from these studies that permeability anisotropy has a significant impact on the fluid flow behaviors under field-scale conditions and thereby could not be ignored, in particular when predicting well productivity after hydraulic fracturing. Moreover, fracture permeability anisotropy varies as the normal stress increases, but it does not exhibit a general rule, which is possibly ascribed to rock heterogeneity. Therefore, fracture permeability anisotropy in rocks is still not fully understood. Especially, little is known about its variation in response to the various normal stresses imposed on the fracture.

Aiming at the issues above-mentioned, the main motivation of the present study is to experimentally examine gas flow behaviors through a rough rock fracture induced by hydraulic fracturing. For comparison, we also adopt the rock fracture created by Brazilian splitting. Before flow testing, we quantitatively evaluate the fracture surface morphology based on a noncontact 3D laser scanner. Then, we test the influence of fracture geometry on nonlinear flow behaviors in both kinds of fractures undergoing a wide range of normal stresses (1.0–40.0 MPa). The injection gas pressure is in the range of 0.1–2.3 MPa. At last, fracture permeability anisotropy is numerically examined for each level of normal stress imposed on the fracture.

2 Theories relevant to this study

In the low-rate flow regime, the flow characteristics in porous media are widely characterized by linear Darcy 's law, as given in Eq. (1):

$$Q = -\frac{kA_h}{\mu}\nabla P \tag{1}$$

where Q is the volume flow rate, [m^3/s]; ∇P is the pressure gradient, [MPa/m]; k is permeability, [m^2]; A_h is flow area perpendicular to the flow direction, [m^2]; μ is the fluid dynamic viscosity coefficient, [Pa·s].

For laminar flow in rock fractures, a parallel plate model is widely adopted to describe Darcy's linear law, which yields the well-known cubic law (Zimmerman et al. 1991; Su et al. 2021):

$$Q = -\frac{we^3}{12\mu}\nabla P \tag{2}$$

where w is the fracture width (perpendicular to the flow direction), [m]; e is the fracture aperture, [m]. Combined Eqs. (1) and (2), $k = e^2/12$ is obtained.

However, considering that the inertial losses induced by the ever-increasing flow rate become non-negligible, nonlinear flow behavior through the fracture would occur. Among the existing empirical models, the Forchheimer formula is commonly used to describe the nonlinear flow behaviors caused by inertial effect and can be expressed as (Zhou et al. 2015):

$$-\nabla P = AQ + BQ^2 \tag{3}$$

where A is the linear coefficient, [kg/s/m^5]; B is the nonlinear coefficient, [kg/m^8]. Both A and B are related to fluid properties and medium geometry. In this study, gas (nitrogen) is adopted for the flow tests. As a result of the strong compressibility of the gas, Eq. (3) cannot be simply applied directly to the data processing. Equation (3) should be transformed into:

$$\frac{dP}{dx} = AQ + BQ^2 = AQ + B'(\rho Q)Q \tag{4}$$

where ρ is fluid density, [kg/m^3]; B' is a nonlinear coefficient (regardless of density), [1/m^5]. Combined with mass conservation (Eq. 5) and the law of ideal gas (Eq. 6), Eq. (3) can be rewritten as Eq. (7).

$$\rho Q = \rho_{out} Q_{out} \tag{5}$$

$$Q = \frac{P_{out} Q_{out}}{P} \tag{6}$$

$$-\frac{P_{in}-P_{out}}{L}=\left(AQ+B'\rho_{out}Q_{out}\right)\frac{2P_{out}Q_{out}}{P_{in}+P_{out}} \tag{7}$$

$$A=\frac{12\mu}{we_h^3} \tag{8}$$

$$B'=\frac{\beta'}{w^2e_h^2} \tag{9}$$

where ρ_{out} is the fluid density at the outlet, [kg/m^3]; Q_{out} is the outlet flow rate, [m^3/s]; B' is the non-Darcy coefficient, [1/m]. A and B' (Chen et al. 2015) can be obtained by fitting the experimental data with the function $f\left(\frac{2P_{out}Q_{out}}{P_{in}+P_{out}},\rho_{out}Q_{out},\left(P_{in}-P_{out}\right)/L\right)$, and then the equivalent hydraulic aperture e_h is obtained according to Eq. (8).

The Reynolds number, Re, defined as the ratio of inertial force to viscous force in the fluid, is widely used to predict the flow behaviors and can be given as (Zimmerman et al. 2004):

$$\mathrm{Re}=\frac{\rho v D_h}{\mu}=\frac{2\rho Q}{\mu w}=\frac{2\rho_{out}Q_{out}}{\mu w} \tag{10}$$

where D_h is the hydraulic diameter, [m]. When the Reynolds number is small, the viscous force dominates over the inertial force and the fluid presents a stable flow state, namely laminar flow. On the contrary, when the Reynolds number is large, the flow field is affected more by the inertial force, and the fluid will show an irregular and unstable flow state, namely turbulent flow. It should be pointed out that the process of fluid flow from laminar flow to turbulent flow is generally called transition flow. The non-Darcy factor α is defined as the ratio of the nonlinear term to the total pressure gradient, which is expressed as:

$$\alpha=\frac{BQ^2}{AQ+BQ^2}=\frac{B'\rho_{out}Q_{out}}{A+B'\rho_{out}Q_{out}} \tag{11}$$

The critical Reynolds number $\left(\mathrm{Re}_c\right)$ has been widely used for characterizing the onset of flow transition to nonlinear and is presented by:

$$\mathrm{Re}_c=\frac{\rho}{\mu w}\frac{A}{B'}\frac{\alpha}{1-\alpha} \tag{12}$$

3 Experimental methodologies

3.1 Sample preparation

To study the flow behaviors in hydraulic fracturing pattern, it is better to use the hydraulic fracturing-induced fractures in situ. However, it is hard to get such fractured rocks for laboratory tests. Hence, the fractures used in this study are manually made by specifical methods. The processes for making fractures are as follows. First, the natural sandstone blocks were cut into cubic samples with a dimension of 200 mm × 200 mm × 200 mm. Then, the cubic samples were fractured with a simple fracturing apparatus and the cylindrical samples were cored along the direction perpendicular to the fracture (Fig. 1a). Finally, the obtained cylindrical samples were divided into the ones with a dimension of ϕ 50 mm × 50 mm and the two ends for each one were exactly polished by a lapping machine. Since this process for making fractures is hard to control, the number of the cylindrical samples is limited (only two were successfully made). In this study, the fractures created by hydraulic fracturing are called HF. For comparison, tensile fractures are created by a self-made Brazilian splitting device using the intact cylindrical samples from the same cubic block (Fig. 1b). In this study, the fractures created by Brazilian splitting are called BS.

3.2 Fracture surface morphology

3.2.1 Fracture surface roughness

To quantitatively evaluate the influence of fracture geometry on flow behaviors, fracture geometries should be measured. A 3D laser profile scanner (Cronos Dual, Open Technologies, Inc., Italy) was utilized for measuring fracture surface topography. Such a scanner could provide high precision (0.1 mm in the x and y coordinates, 0.02 mm in the z coordinate), high measurement speed and favorable repeatability. After scanned, the topography data were then input into the open-source software ParaView 5.6.0 (Kitware Inc., USA, a program designed for multi-platform data analysis and visualization) to reproduce the 3D rough surface of each fracture. Figure 2 shows the 3D surface topography of each sample. As shown

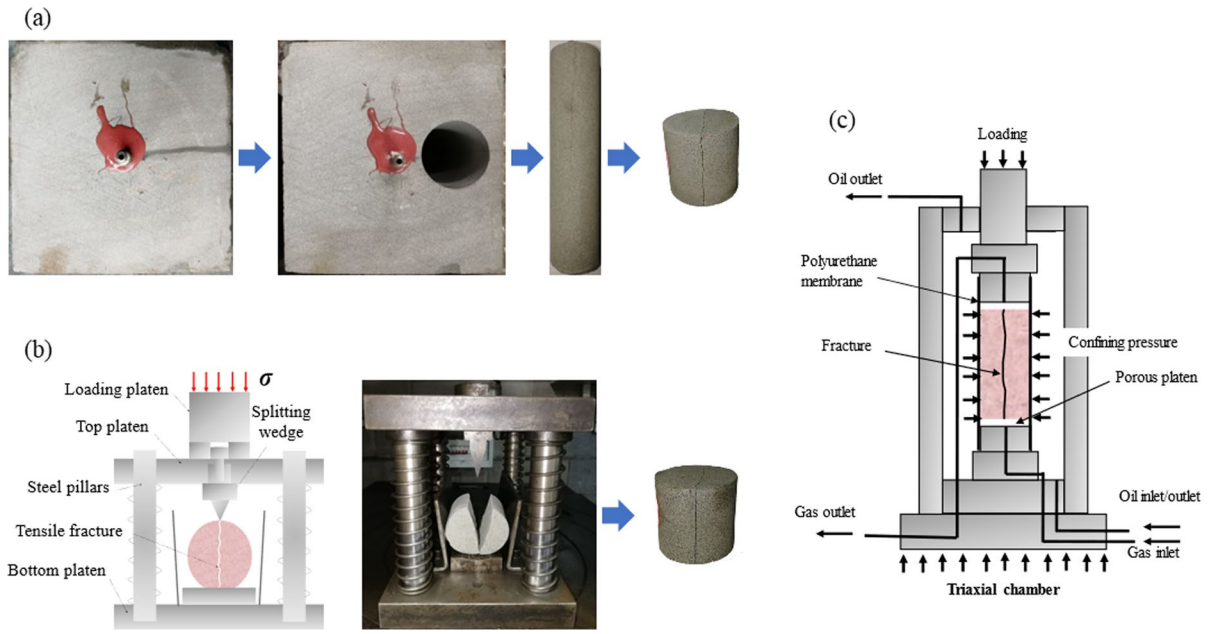

Fig. 1 **a** The generation process of hydraulic fractures; **b** the generation process of splitting fractures with a Brazilian splitting device; **c** triaxial apparatus for gas flow tests

in Fig. 2, the x direction represents the flow direction and fracture asperity is indicated by the color bar. The two surfaces for one fracture are very similar, but their maximum magnitudes of asperity are not the same. The main reason for this phenomenon is that rock fragments ejected or fell off during the fracture making process. It is obvious that the ranges of asperity for BS1 and BS2 are larger than those for HF1 and HF2.

To quantitatively describe the fracture surface roughness, two parameters (R_p, Z_2) (Myers 1962; Maerz et al. 1990; Jang et al. 2014) are directly adopted for analyzing the scanned data and are given as:

$$R_p = \frac{\sum_{i=1}^{N} \sqrt{(dx_i)^2 + (dz_i)^2}}{L} \tag{13}$$

$$Z_2 = \frac{1}{L}\sqrt{\int_{x=0}^{x=L} \left(\frac{dz}{dx}\right)^2 dx} = \sqrt{\frac{1}{Ndx^2}\sum_{i=1}^{N}(dz_i)^2} \tag{14}$$

where R_p is roughness profile index, [–]; N is the number of data points in one profile line, [–]; dx_i, dz_i are respectively the distance between points along and perpendicular to profile line, [m]; Z_2 is the root mean square of the fracture profile wall slope, [–]. These parameters are averaged over ten uniformly spaced profiles along the flow direction for one fracture surface. Figure 3 gives two examples of the ten profiles for calculating R_p and Z_2, for hydraulic fracturing and splitting, respectively. It is seen in Fig. 3 that the profiles for splitting fluctuates more seriously and tortuously. The calculated results show that R_p ranges from 1.0431 to 1.0442 for splitting fractures and from 1.0366 to 1.0382 for hydraulic ones; Z_2 ranges from 0.280 to 0.333 for splitting fractures and from 0.250 to 0.319 for hydraulic ones. This implies that the fractures created by hydraulic fracturing are relatively smoother than those made by splitting.

3.2.2 *Aperture distribution*

Fracture aperture is positively corelated with its hydromechanical behaviors (Nemoto et al. 2009; Brown et al. 1986; Kulatilake et al. 2008; Ye et al. 2017), which is often defined as the distance between two corresponding points located at each fracture surface. Based on the classic cubic law, the aperture size is constant between two parallel smooth plates. Since in reality the fracture surface is rough, the aperture size varies at each measured location. An algorism

(a) BS1-side 1

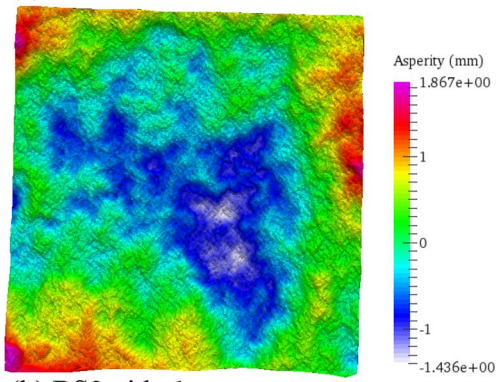

(e) BS1-side 2

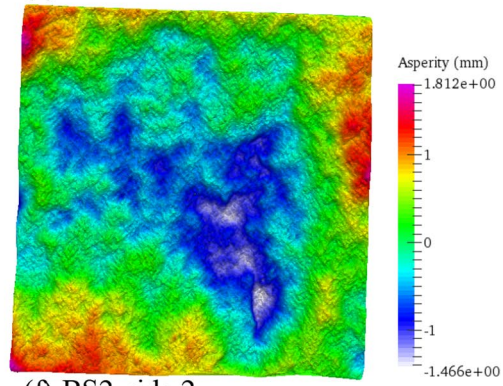

(b) BS2-side 1

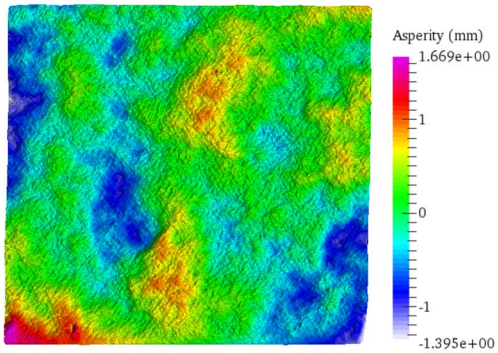

(f) BS2-side 2

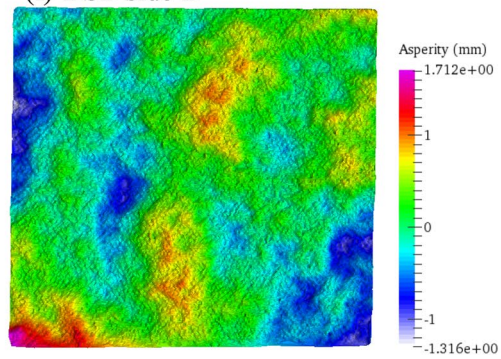

(c) HF1-side 1

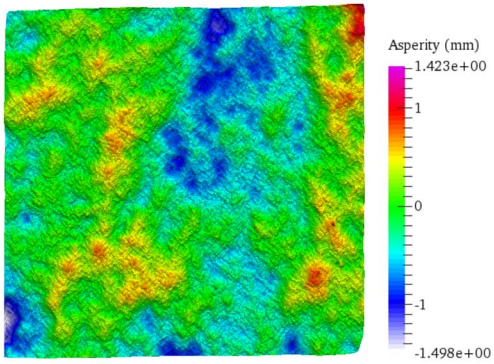

(g) HF1-side 2

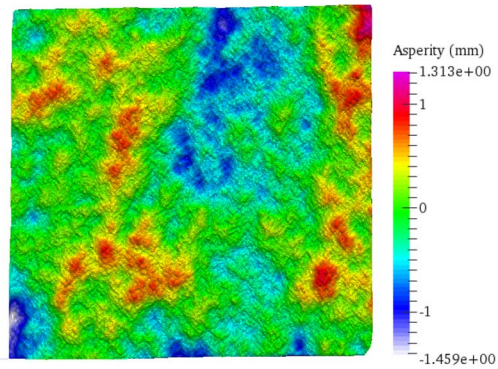

(d) HF2-side 1

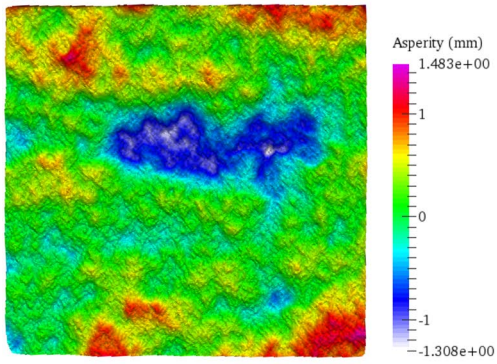

(h) HF2-side 2

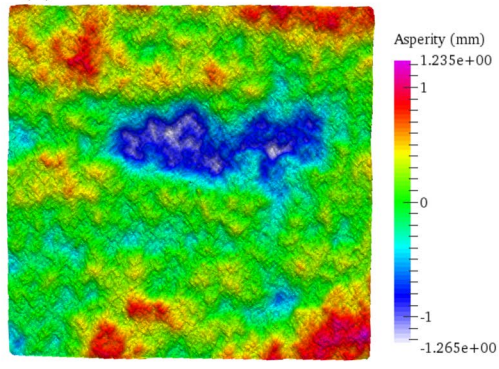

◂**Fig. 2** 3D digital surface topography of each sample based on a scanner

for the process of the scanned data in Fig. 2 was utilized to make the two fracture surfaces matched well. A geometrical model, whose size is the same as the experimentally used fracture, was constructed in Flac3D. Then, based on the scan laser's accuracy in x and y directions, the model was meshed into discrete zones at a spatial density. After that, each zone has an aperture by implementing into the scanned topography data. More details can be found in Shen et al. (2020). Figure 4 plots the flow chart to calculate aperture of each zone. For element i, according to the four nodes on each side of the fracture, the aperture size is calculated as

$$a_i = \frac{1}{4}\left[\left(h_{i5} - h_{i1}\right) + \left(h_{i6} - h_{i2}\right) + \left(h_{i7} - h_{i3}\right) + \left(h_{i8} - h_{i4}\right)\right] \quad (15)$$

where a_i is the calculated aperture size for the element i, [m]. Note that if the aperture of the element is smaller than zero, the element is defined as contact. The contact ratio is defined as the ratio of the number of contact elements to that of the total elements. In this study, it is assumed that the contact ratio be 1% for the initial state (zero normal stress).

Figure 5 depicts the calculated aperture distribution and the best-fitted curves for each sample based on the Gaussian model. The best-fitted coefficients are listed in Table 1. As demonstrated in Fig. 5, the peak frequency is about 4.6% for BF1, 7.2% for BF2, 7.96% for HF1, and 7.97% for HF2, respectively; the mean aperture size is approximately 0.223 mm for BF1, 0.164 mm for BF2, 0.127 mm for HF1, and 0.121 mm for HF2, respectively. On the whole, aperture distributions for splitting fractures (BS1, BS2) are broader with lower peak frequency whereas they are narrow with large peak frequency for hydraulic ones (HF1, HF2) showing a concentrated distribution characteristic.

3.3 Testing procedure for gas flow tests

The gas flow tests were conducted using a servo-controlled triaxial system (Fig. 1c). The testing system contains a triaxial cell with servo-controlled axial and lateral loading system. The gas pressure is applied by nitrogen gas cylinder from the bottom to the top of the fracture and is measured by an electronic flowmeter at the outlet, which is directly exposed to the atmosphere. During the testing, the effective confining pressure, defined as the value that the total confining pressure minus the average of the inlet and outlet gas pressures, was progressively increased from 1 to 40 MPa. At each effective confining pressure, the inlet gas pressures ranging from 0.1 to 2.3 MPa were imposed. Note that the inlet pressure is always designed to be lower than the confining pressure to avoid sealing failure and sample collapse. For a given combination of confining pressure and inlet pressure, the discharge was recorded when the gas flow at the outlet was stabilized.

3.4 Results

All the tests are performed under isothermal room temperature. In the following analysis, the density of gas is taken as 1.16×10^3 kg/m^3 and viscosity 1.758×10^{-5} Pa·s. Due to the low permeability (10^{-17} m^2) of rock matrix, the gas was assumed to flow only through the fracture.

3.4.1 Flow rate versus pressure gradient

Figure 6 shows the relationship between the flow rate and pressure gradient for gas flow through four fractures subjected to confining pressure ranging from 1 to 40 MPa. It can be seen that for each curve, the flow rate rises linearly with the increase of the pressure gradient at the beginning, and then doubling the pressure gradient does not produce double flow rate, indicating the occurrence of the nonlinear flow. This is primarily due to the non-negligible inertial effect caused by the ever-increasing gas flow rates. As the confining pressure increases, the nonlinearity becomes less evident, which is mainly ascribed to the decrease in flow rate induced by the less void space under high levels of confining pressure. It seems that the splitting fractures exhibit stronger nonlinearities, showing that their curves are steeper for a given confining pressure. This may be due to more void space caused by their lower matching degree of the two fracture walls.

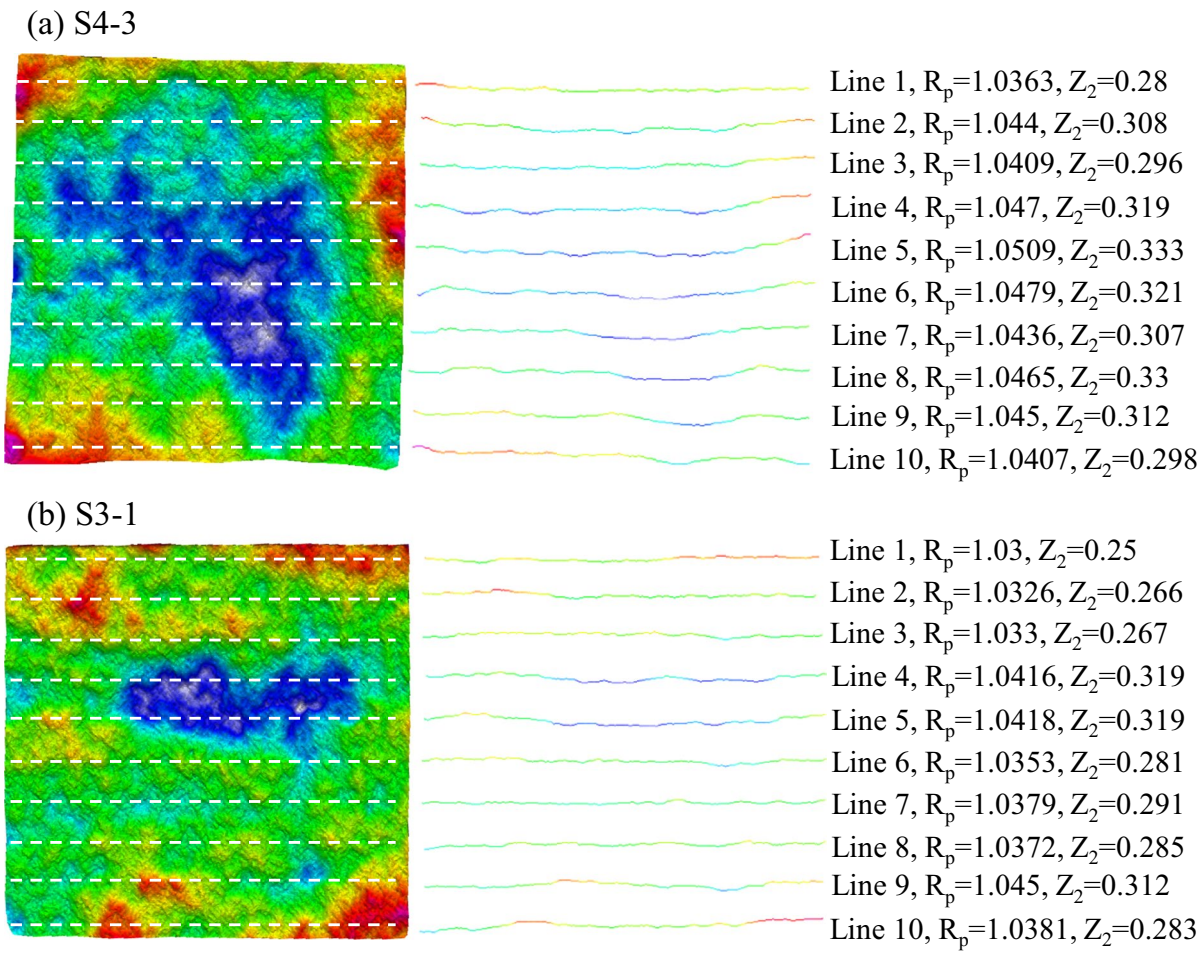

Fig. 3 Two examples of ten profiles and the corresponding calculated R_p and Z_2 values

3.4.2 Stress-dependent hydraulic characteristics

For fluid flow through the fracture, apparent transmissivity has been utilized for evaluating the nonlinear flow regime (Zimmerman et al. 2004; Yin et al. 2017; Zhou et al. 2016; Wang et al. 2020) and it is defined as:

$$-\nabla P = \frac{\mu}{T} Q \tag{16}$$

where T is the apparent transmissivity, [m^4]. If the nonlinearity can be neglected, the apparent transmissivity would be regarded as the real transmissivity of the fracture. Figure 7 plots the calculated apparent transmissivity as a function of Reynolds number at each combination of confining pressure and inlet gas pressure. It is clear that the apparent transmissivity does not remain unchanged but follows a decreasing tendency with the increase in Reynolds number. This further confirms the occurrence of the nonlinearity. Table 2 lists the ranges of transmissivity at different confining pressures for each fracture. Overall, transmissivity decreases by two orders of magnitude with σ_c increasing for splitting fractures while by three orders of magnitude for hydraulic fractures. It is worth noting that for a higher σ_c, the range of transmissivity is smaller and the corresponding curve becomes linear. This phenomenon occurs at a relatively smaller σ_c for hydraulic fractures, indicating that the nonlinearities in hydraulic fractures are less evident than that of splitting fractures.

For convenience in comparison, the raw experimental data need be first processed using Eq. (7) and best-fits with high fitting coefficients over 0.99

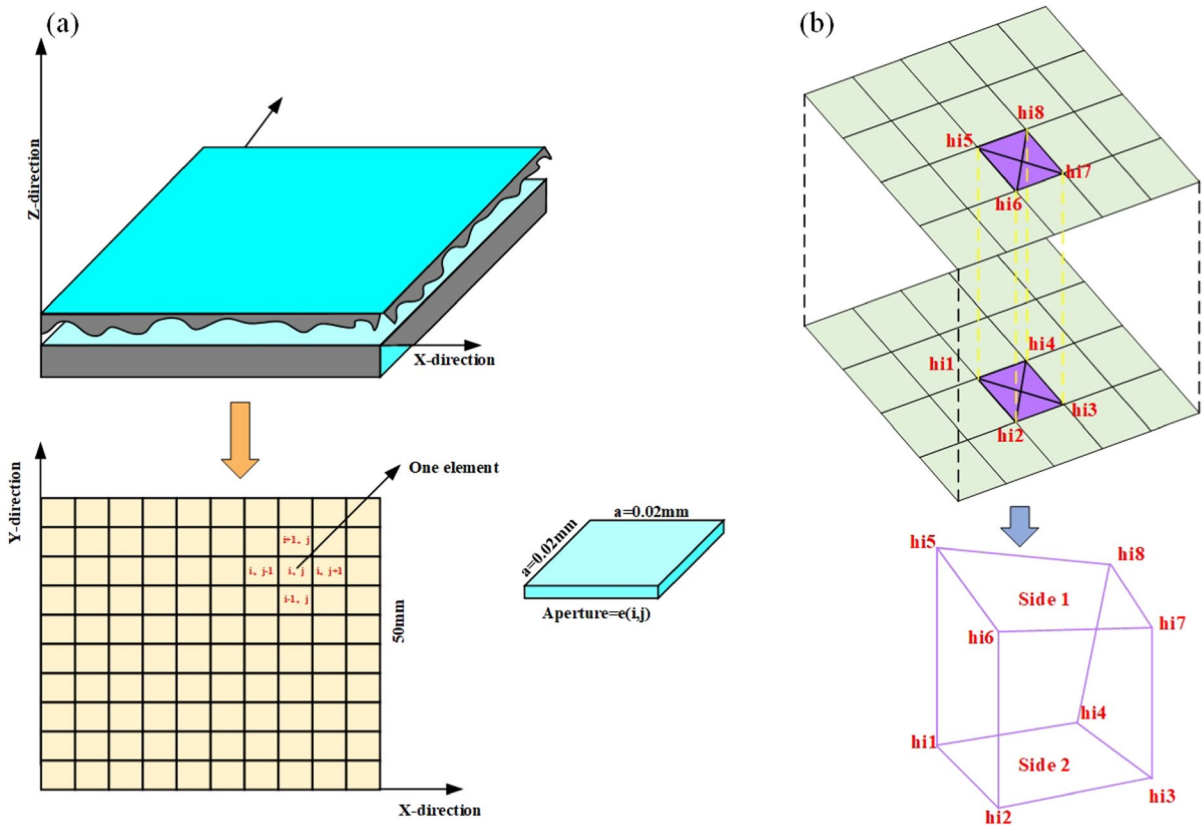

Fig. 4 Calculation process of fracture aperture distribution: **a** geometrical model of fracture; **b** calculating method for one zone

determination are acquired. The obtained best-fitted parameters A and B' for each confining pressure are illustrated in Fig. 8. It depicts that both linear coefficient A and nonlinear coefficient B' increase as the confining pressure rises. Both A and B' for hydraulic fractures are approximately two orders of magnitude larger than those for splitting fractures.

Based on the calculated A, the intrinsic transmissivity ($T_0 = \mu/A$) could be obtained. Figure 9 shows the intrinsic transmissivity of the four fractures. As shown in Fig. 9, the intrinsic transmissivity T_s for splitting fractures is much larger than that of hydraulic fractures T_f, especially under high levels of confining pressure. Both T_s and T_f decrease with the confining pressure, but T_f possesses a larger reduction rate. The average T_s ranges from 1.51×10^{-16} m^4 at $\sigma_c = 1$ MPa to 1.19×10^{-18} m^4 at $\sigma_c = 40$ MPa whereas 6.02×10^{-17} m^4 at $\sigma_c = 1$ MPa to 1.95×10^{-20} m^4 at $\sigma_c = 40$ MPa for T_f. The ratio of T_s to T_f increases from 2.51 at $\sigma_c = 1$ MPa to 60.95 at $\sigma_c = 40$ MPa.

In order to quantify the intrinsic transmissivity reduction for a given loading stress, the relative intrinsic transmissivity reduction rate R_T is introduced as:

$$R_T = \frac{T_{0i} - T_{0c}}{T_{0i}} \times 100\% \tag{17}$$

where T_{0i}, T_{0c} represents the fracture intrinsic transmissivity for the initial state (1 MPa) and current confining pressure, respectively, [m^4]. The calculated R_T for each loading stress is plotted in Fig. 10. The average R_T increases sharply at first and remain almost constant until a certain confining pressure is reached. In general, R_T for hydraulic fractures is relatively larger. For example, $R_T \approx 99\%$ occurs at $\sigma_c = 30$ MPa for splitting fractures while at $\sigma_c = 16$ MPa for hydraulic fractures.

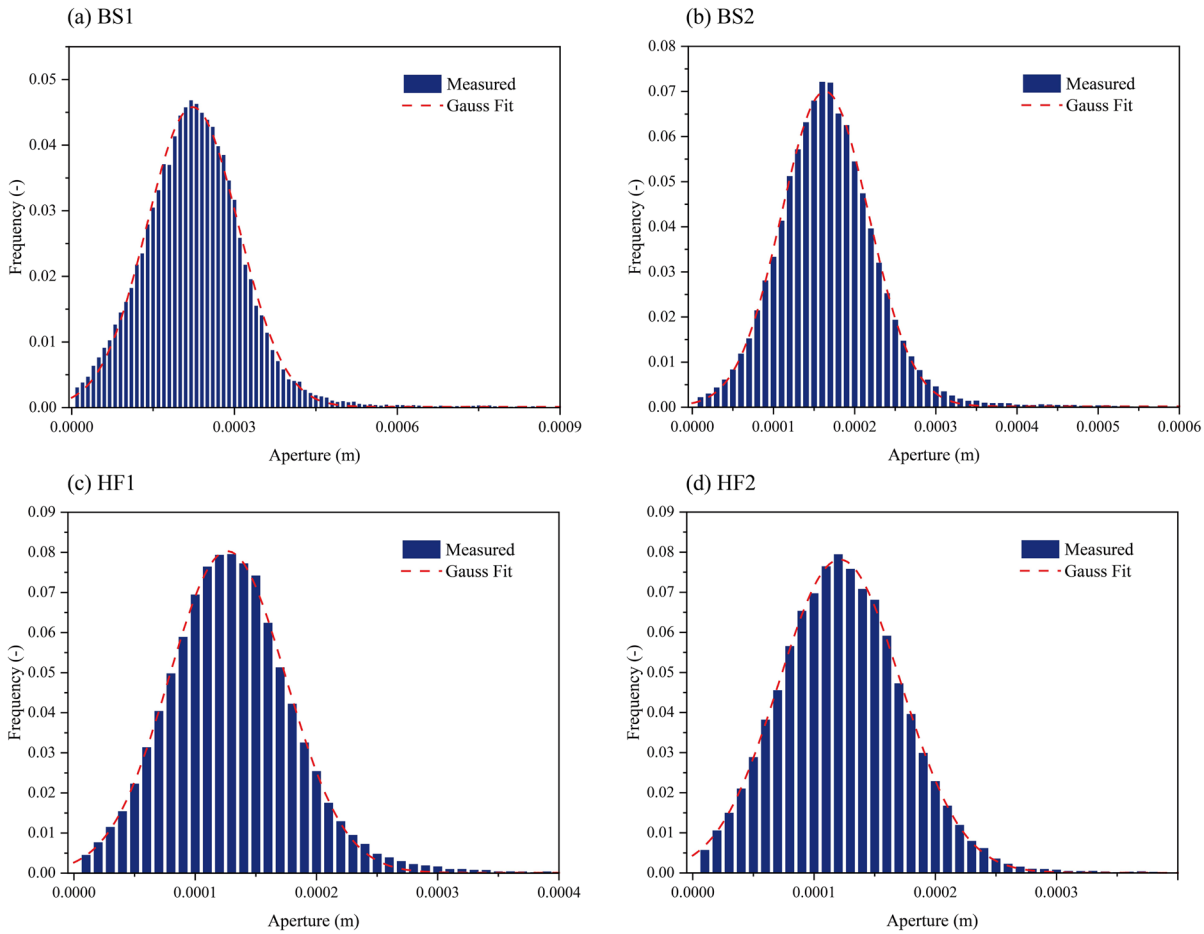

Fig. 5 Aperture distribution and the best-fitted curve for each fracture: **a** BS1; **b** BS2; **c** HF1; **d** HF2

Table 1 The best-fitted coefficients of aperture distribution for each fracture

Model $f(x) = \frac{1}{\sqrt{2\pi}\lambda}\exp\left(-\frac{(x-\eta)^2}{2\lambda^2}\right)$					
Sample	η (mm)	Average η (mm)	λ (mm)	Average λ (mm)	R^2 (–)
BS1	0.2229	0.19320	0.1687	0.13845	0.99716
BS2	0.1635		0.1082		0.99870
HF1	0.1266	0.12395	0.09647	0.098585	0.99878
HF2	0.1213		0.1007		0.99904

3.4.3 Critical Reynolds number and pressure gradient

The critical Reynolds number Re_c defines the onset of nonlinear flow. In engineering practice, the nonlinear effect can be appreciable and not be neglected if the nonlinear term (BQ^2) accounts for over 10% of the pressure drop, namely $E = 0.1$ (Zimmerman et al. 2004; Zhou et al. 2015; Javadi et al. 2014). Based on Re_c, the linear and nonlinear flow regimes can be explicitly distinguished. The fluid flow in the fractures can be assumed to be laminar if Reynolds number is smaller than Re_c. According to Eq. (12), Re_c of the four fractures are calculated for each

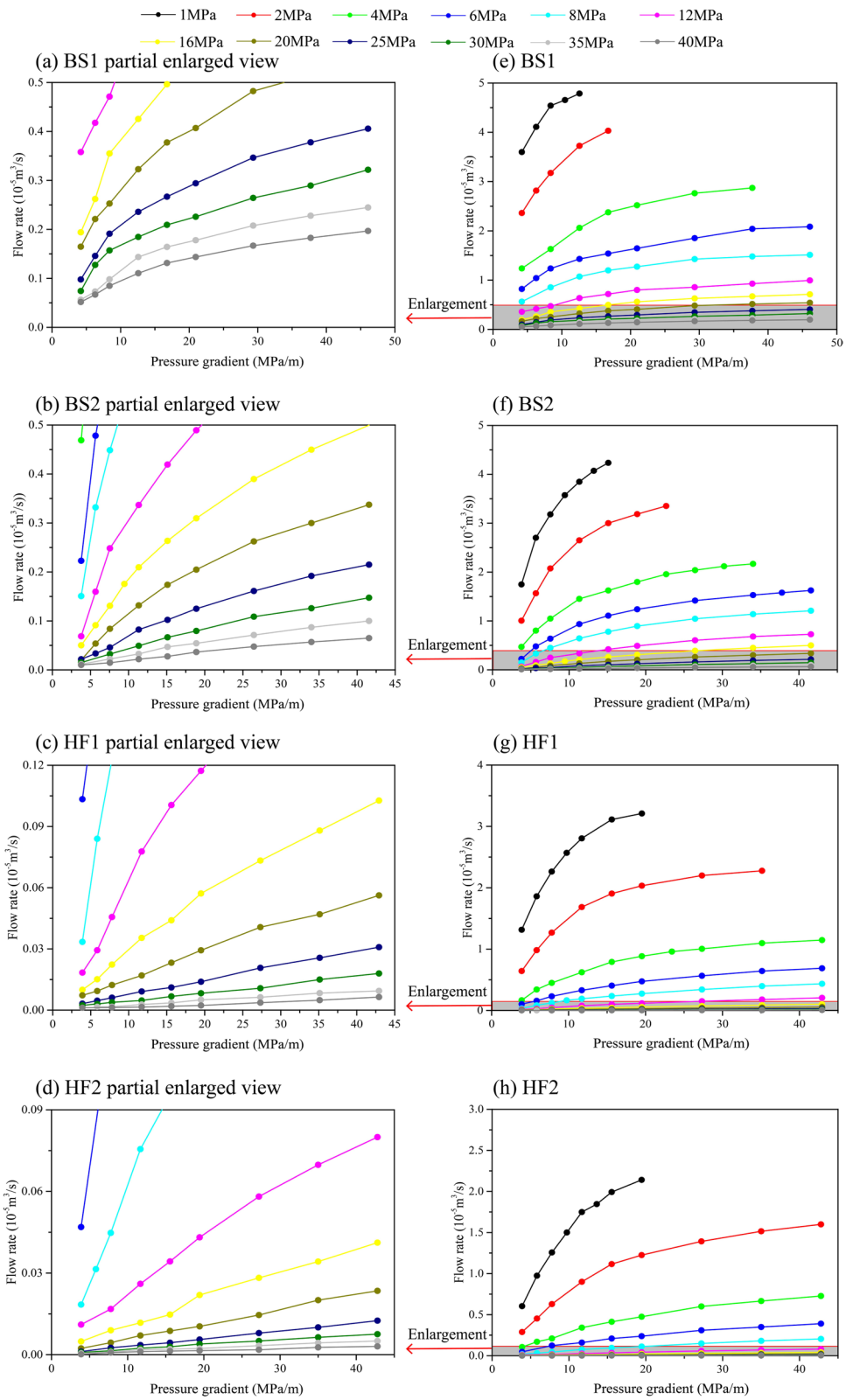

Fig. 6 The relationship between flow rate and pressure gradient for each fracture: **a–d** partial enlarged view; **e–h** normal view

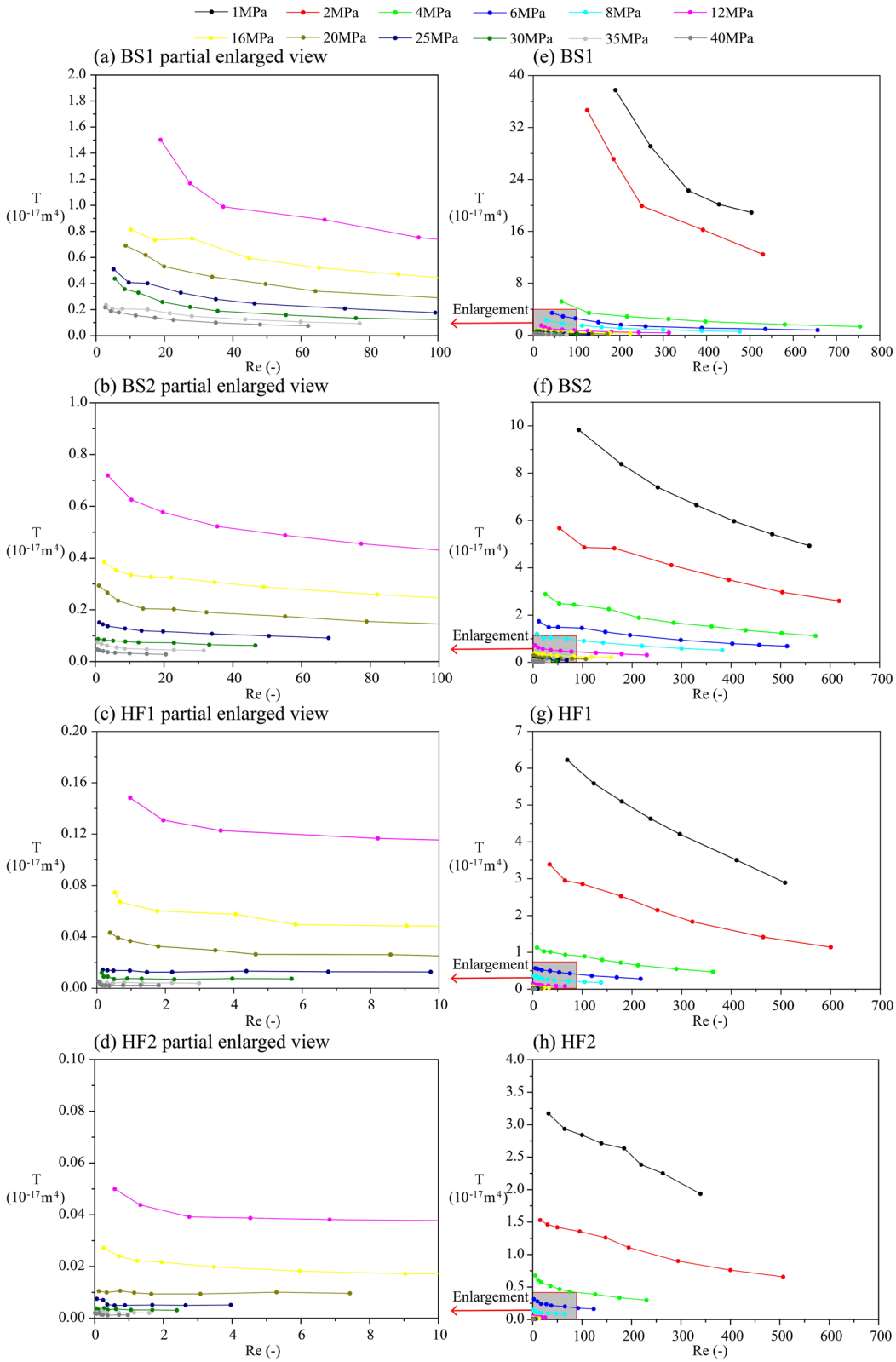

Fig. 7 The relationship between apparent transmissivity and Reynolds number for each fracture: **a**–**d** partial enlarged view; **e**–**h** normal view

Table 2 The ranges of transmissivity at different confining pressures for each fracture (1 MPa, 40 MPa)

Sample	Transmissivity/10^{-17} m^4	
	$\sigma_c = 1$ MPa	$\sigma_c = 40$ MPa
BS1	3.27-18.9-	0.217–0.075
BS2	8.13–4.93	0.0468–0.0275
HF1	5.92–2.89	0.00514–0.00234
HF2	2.73–1.93	0.00199–0.00125

confining pressure and are shown in Fig. 11. It can be seen that Re_c for the four fractures BS1, BS2, HS1 and HS2 falls within a range of 2.67–0.43, 1.37–0.23, 1.78–0.24 and 1.72–0.28, respectively, subjected to the confining pressure from 1 to 40 MPa. On the whole, Re_c decreases with increasing the confining pressure for each fracture and Re_c for splitting fractures is larger.

Substituting Eq. (10) into (3), the pressure gradient as a function of Reynolds number is given as (Zhou et al. 2015):

$$-\nabla P = A\left(\frac{\mu w}{\rho}\mathrm{Re}\right) + B\left(\frac{\mu w}{\rho}\mathrm{Re}\right)^2 \tag{18}$$

Combining with Eqs. (5) and (6), the pressure gradient can be calculated. Figure 12 plots the flow regimes in the full range of confining pressure for the four fractures. The solid curves are the theoretical results based on Eq. (18) and the scatter points are the experimental data. The whole flow zone is divided

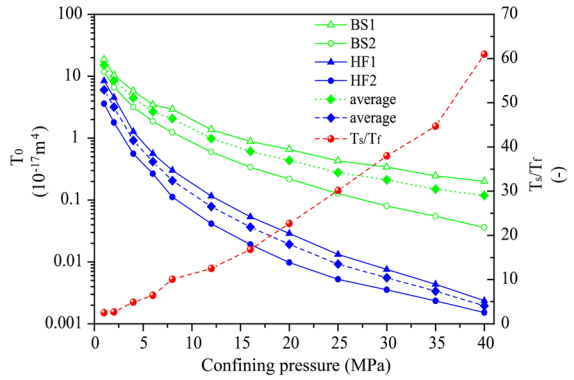

Fig. 9 Comparisons of the intrinsic transmissivity for splitting and hydraulic fractures with the increase of confining pressure from 1 to 40 MPa

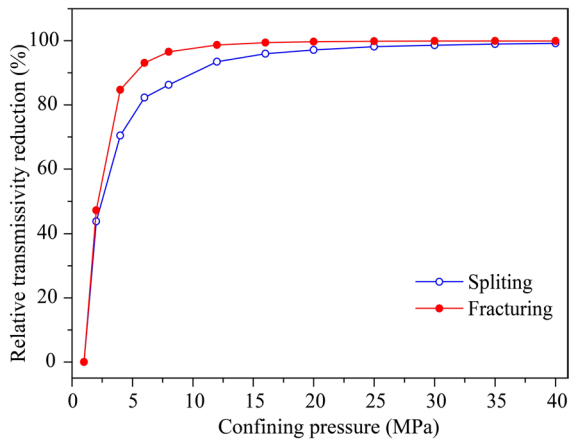

Fig. 10 The calculated intrinsic transmissivity reduction rates of splitting and hydraulic fractures for each confining pressure

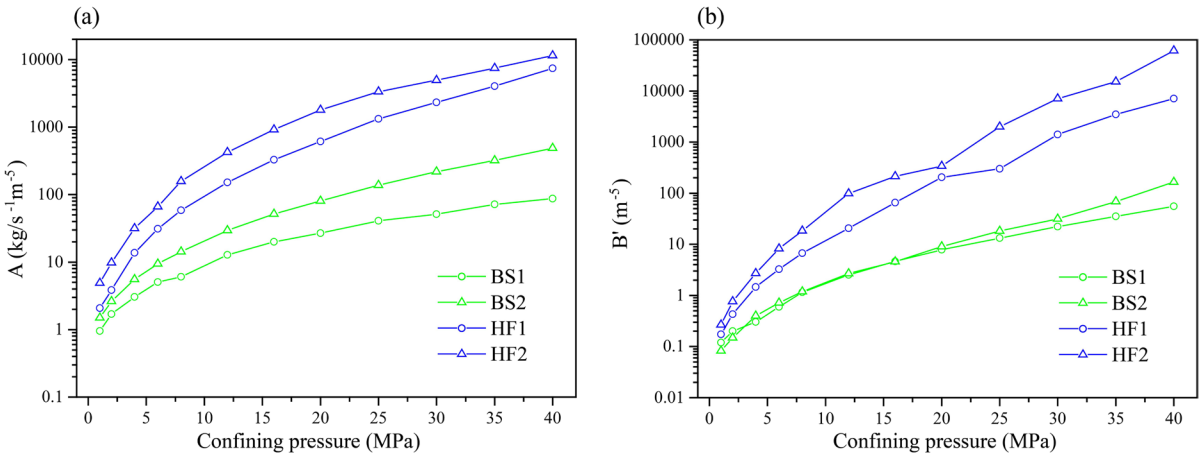

Fig. 8 The best-fitted parameters A and B' based on Forchheimer equation for each fracture with the increase of confining pressure from 1 to 40 MPa

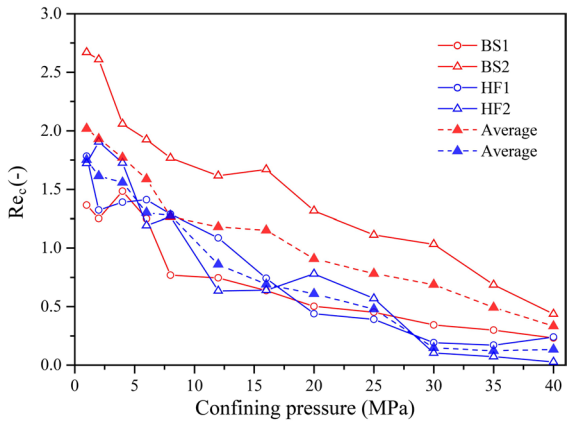

Fig. 11 Comparisons of the critical Reynolds numbers for splitting and hydraulic fractures with the increase of confining pressure from 1 to 40 MPa

into a linear zone and a nonlinear zone by a critical line determined by Re_c using Eq. (18). The results indicate that the critical line is actually a curve with varying Re_c, instead of a vertical line with unchanged Re_c. All the experimental data for $\sigma_c = 1$ MPa are located in the nonlinear zone, implying that nonlinearity could easily occur at low levels of confining pressure. As for the case at $\sigma_c = 40$ MPa, all the points for splitting fractures stay in the range of the nonlinear zone while for hydraulic fractures, some points appear in the linear zone. This indicates that the decrease in fracture aperture caused by high confining pressure is more significant in hydraulic fractures so that the channels for flow are limited more and the flow rate is relatively smaller. As a result, the flow turns into linearity. Figure 13 compares the critical pressure gradient in the full range of the confining pressure for the four fractures. As illustrated in Fig. 13, the critical pressure gradient increases as the confining pressure rises, indicating that more energy is required for the occurrence of nonlinearity at high levels of the confining pressure. This is in good agreement with the experimental observations in Fig. 6. Apparently, the critical pressure gradients for hydraulic fractures are generally larger, which implies that the occurrence of nonlinearity is more difficult in hydraulic fractures. For instance, at $\sigma_c = 40$ MPa, the average critical pressure gradient is about 0.91 MPa/m for hydraulic fractures while approximately 0.088 MPa/m for splitting ones.

Figure 14 presents the comparisons of Re for the four fractures at $\sigma_c = 2$ MPa, 8 MPa, 20 MPa, 40 MPa, respectively. It can be seen that with the increase of confining pressure, Re gradually decreases. Totally, when the confining pressure varies from 2 to 40 MPa, Re decrease by two orders of magnitude for the hydraulic fractures while by one order of magnitude for the splitting ones. Note that at each confining pressure, Re for the splitting fractures are clearly larger under the same gas inlet pressure, which is the main reason for that the splitting fractures possess stronger nonlinearities in comparison of hydraulic ones.

3.4.4 Normalized transmissivity

In order to further examine the nonlinear flow regime in the rock fractures, normalized transmissivity is determined in the following form (Zimmerman et al. 2004):

$$\frac{T}{T_0} = \frac{1}{1 + \beta Re} \tag{19}$$

where β is the dimensionless Forchheimer coefficient, [–]. The normalized transmissivity against Reynolds number for each fracture is plotted in Fig. 15. As a whole, T/T_0 decreases with the increase in Re. At low Re, T/T_0 fluctuates around 1. As Re rises, the scatter points of T/T_0 start to bend down, which is caused by the increase of inertial force. When a critical Re is reached, T/T_0 decreases sharply because of the dominated inertial effect. The results indicate that the flow behaviors are strongly dependent on the value of Re. $T/T_0 = 0.9$ is often adopted for defining the boundary line where the nonlinear effect becomes significant (Zimmerman et al. 2004; Zhou et al. 2015; Javadi et al. 2014). It is noticed that most of the scatter points for splitting fractures are located in the zones ($T/T_0 < 0.9$) while in the zones ($T/T_0 > 0.9$) for hydraulic ones, which demonstrates that the nonlinear effect is stronger in splitting fractures. Moreover, the best-fitted curve by Eq. (19) of experimental data for each fracture is also given in Fig. 15. The coefficient β for splitting fractures locate at 0.00643, 0.00517, respectively, larger than that of hydraulic ones (0.00471, 0.00337). This also validates that stronger nonlinearity occurs in the splitting fractures. All the experimental normalized transmissivity data

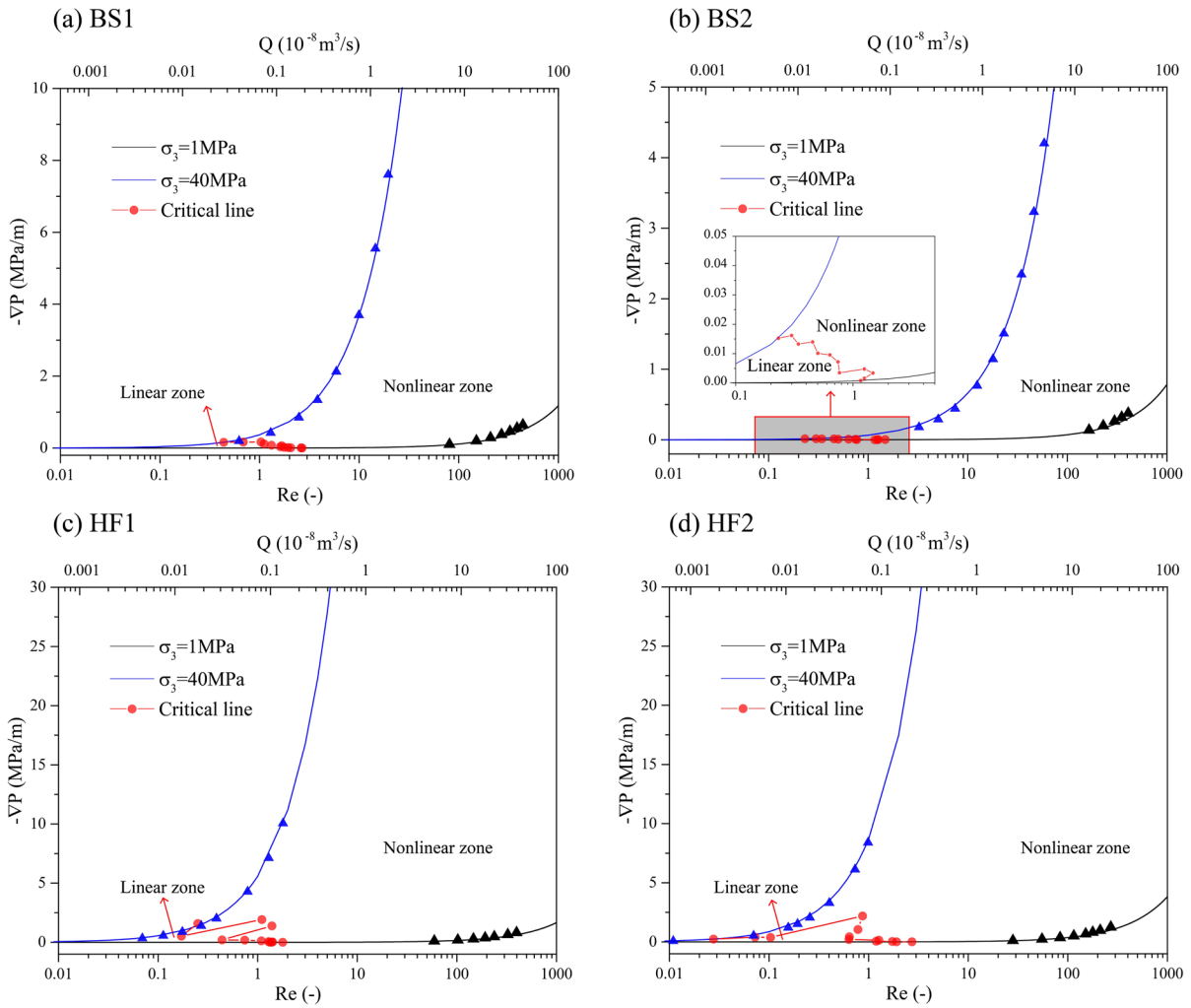

Fig. 12 Flow regime distribution in splitting and hydraulic fractures: **a** BS1; **b** BS2; **c** HF1; **d** HF2

for the splitting and hydraulic fractures and the corresponding best-fitted curves by Eq. (19) are illustrated in Fig. 16. The coefficient β of splitting fractures (0.00577) is almost 1.5 times than that of hydraulic ones (0.0041).

Furthermore, Eq. (20) (rearranged from Eq. (19)) can be utilized to check whether the nonlinear effect occurs and expressed as (Zimmerman et al. 2004):

$$\frac{T_0/T-1}{Re}=\beta \tag{20}$$

If the data points based on Eq. (20) fall on a straight line, it indicates that a weak inertial effect occurs; if the relationship between the pressure drop versus flow rate is nonlinear, the data points usually fall on a horizontal line for each confining pressure. Figure 17 illustrates the relationship between Re and $\left(T_0/T-1\right)$ for each fracture. As a whole, the data is distributed over a wide range and it is hard to catch any information at low value of Re, especially for the hydraulic fractures. With the enlargement of each figure, it is clearly observed that on the whole, for a given confining pressure, the data points first locate on the ascending or descending line and then level off to a constant value. For BS1, the data points initially exhibit an ascending trend and then gradually level off to a constant value; for HS1 and HS2, these data first present a descending trend and then gradually level off to a constant value. As for BS2, under low confining pressures, the data first shows an

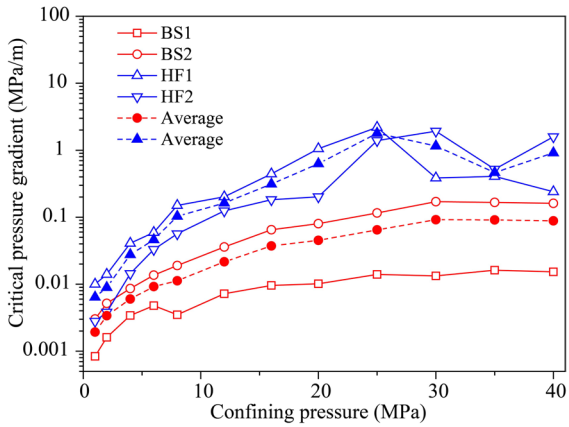

Fig. 13 Comparisons of the critical pressure gradients for splitting and hydraulic fractures with the increase of confining pressure from 1 to 40 MPa

ascending trend and then level off while descending and then leveling off for high confining pressures. It seems that the characteristics of these curves are strongly related to Re. At low Re, the curves are prone to first descend/ascend before leveling off for high Re.

4 Permeability anisotropy based on numerical simulation

Due to the limitation of our testing system and the cylindrical samples, it is difficult to experimentally examine the permeability anisotropy in different

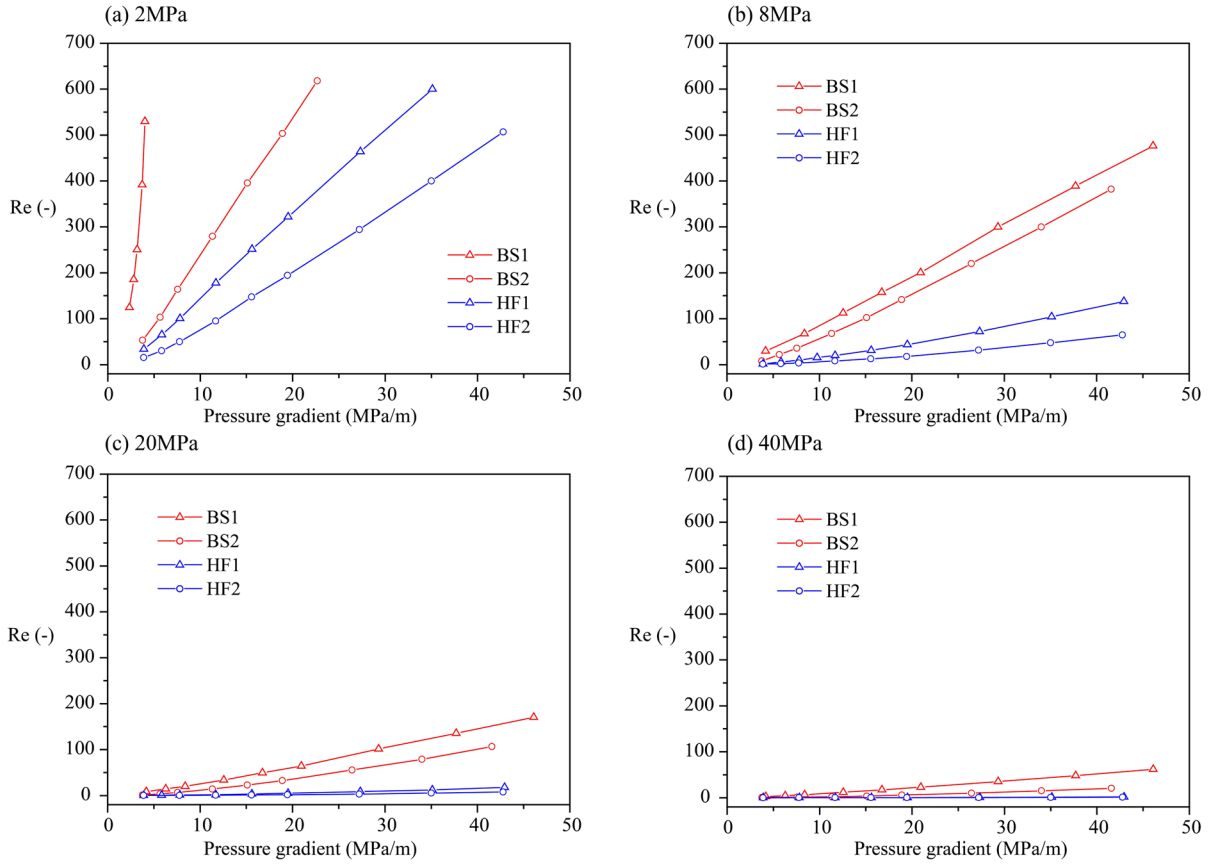

Fig. 14 Comparisons of Reynolds numbers for splitting and hydraulic fractures under different confining pressures: **a** $\sigma_c = 2$ MPa; **b** $\sigma_c = 8$ MPa; **c** $\sigma_c = 20$ MPa; **d** $\sigma_c = 40$ MPa

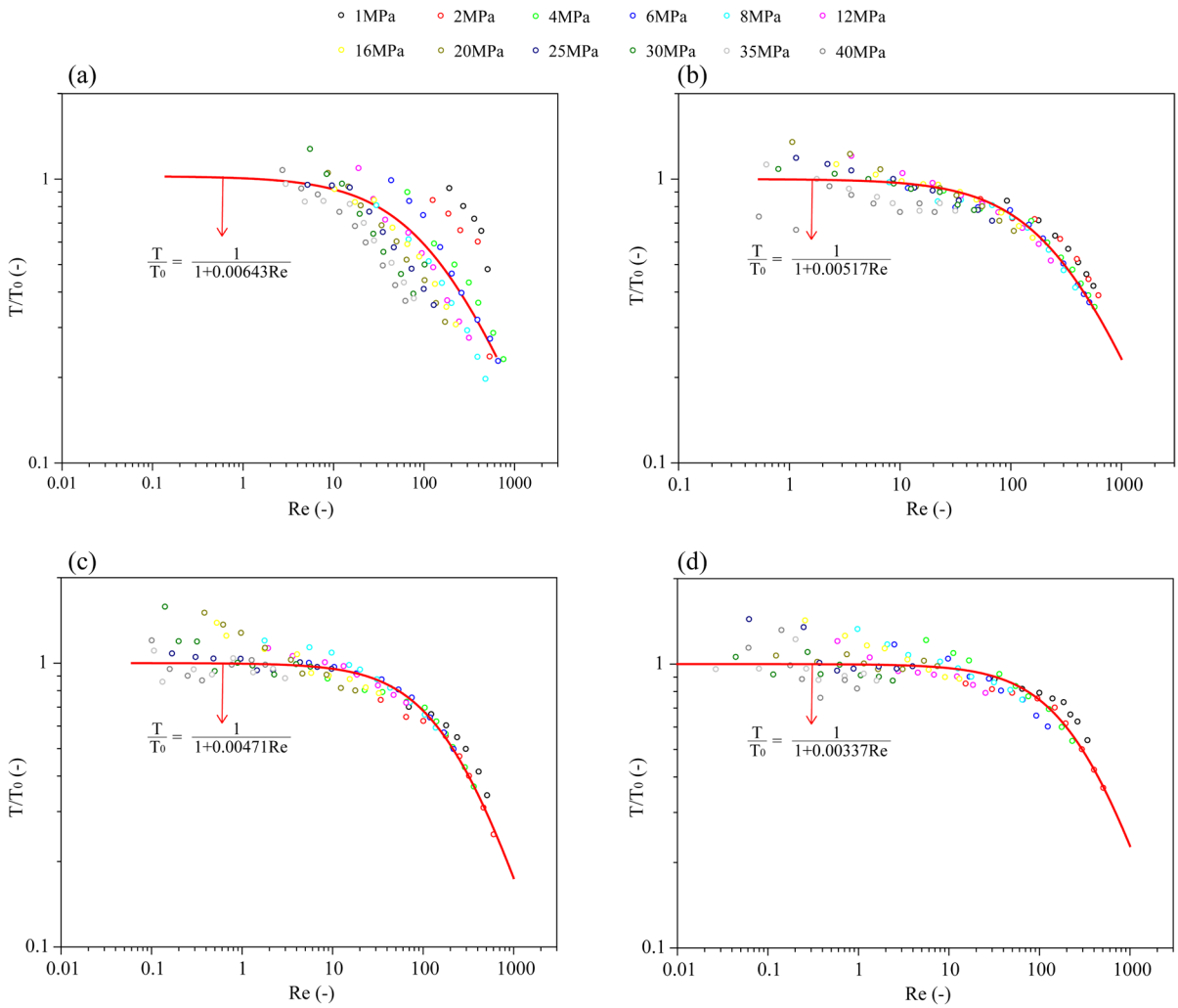

Fig. 15 The relationship between normalized transmissivity and Reynolds number for each fracture: **a** BS1; **b** BS2; **c** HF1; **d** HF2

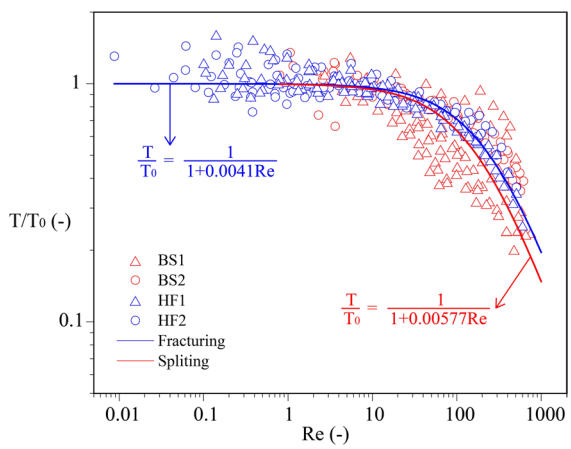

Fig. 16 Comparisons of normalized transmissivity for splitting and hydraulic fractures

directions. Therefore, numerical simulation is adopted for this topic.

4.1 Modeling setup

A geometric model of rock fracture with aperture distribution is the same as that in Sect. 3.2.2. The geometric model is divided into 250×250×1 homogeneous hexahedral zones, as shown in Fig. 18.

In numerical simulation, the fluid flow in rock fracture is simplified as a pseudo 3D issue based on the aperture distribution. A 2D pressure governing equation Eq. (21), which contains mass conservation and cubic linear law, is utilized for the stationary

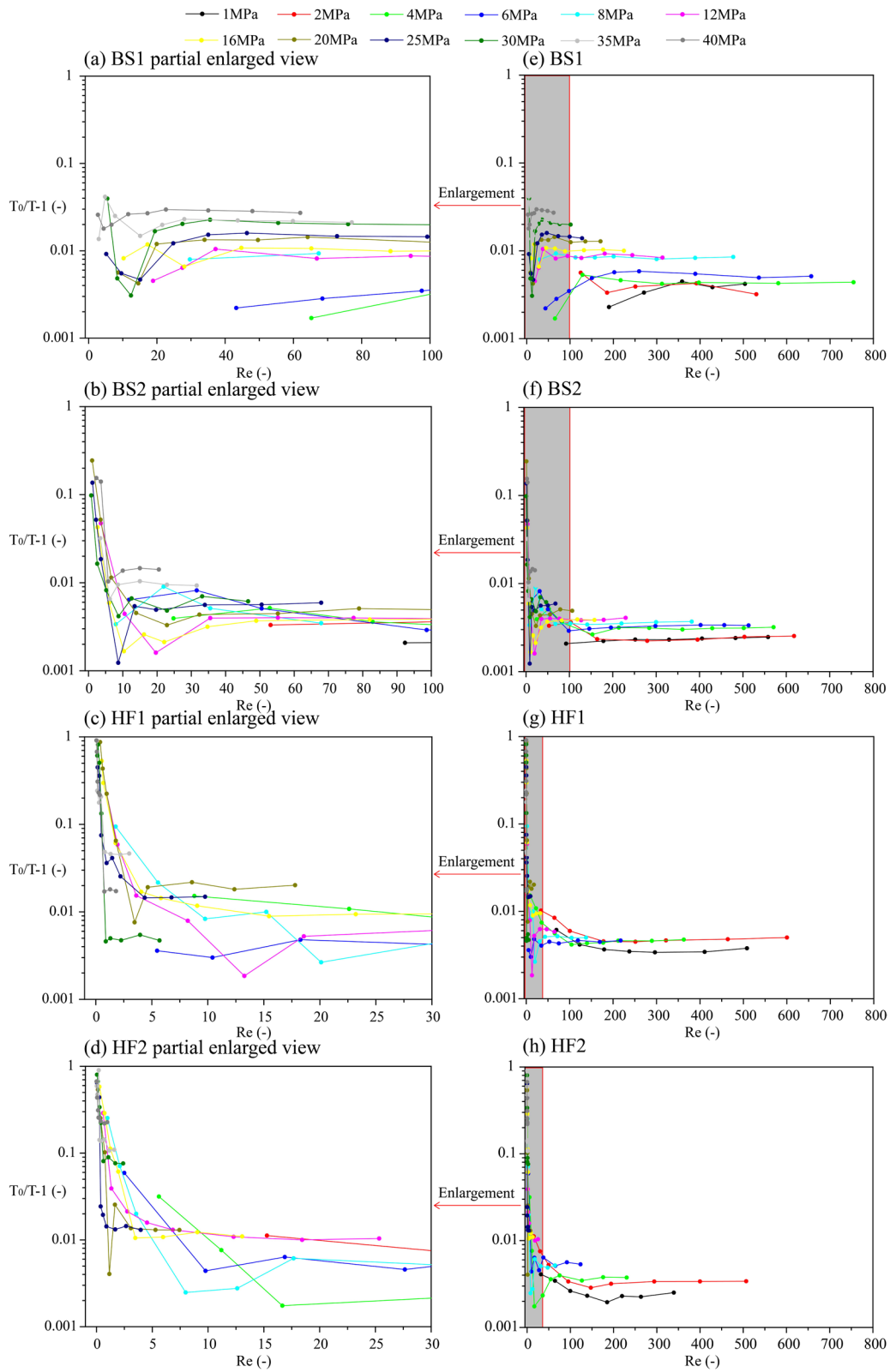
1MPa
2MPa
4MPa
6MPa
8MPa
12MPa
16MPa
20MPa
25MPa
30MPa
35MPa
40MPa
(a) BS1 partial enlarged view
(e) BS1
(b) BS2 partial enlarged view
(f) BS2
(c) HF1 partial enlarged view
(g) HF1
(d) HF2 partial enlarged view
(h) HF2
Enlargement
T0/T-1 (-)
Re (-)

◂**Fig. 17** Variations in $T_0/T-1$ in response to the increase in Reynolds number for each fracture: **a**–**d** partial enlargeview; **e**–**h** normal view

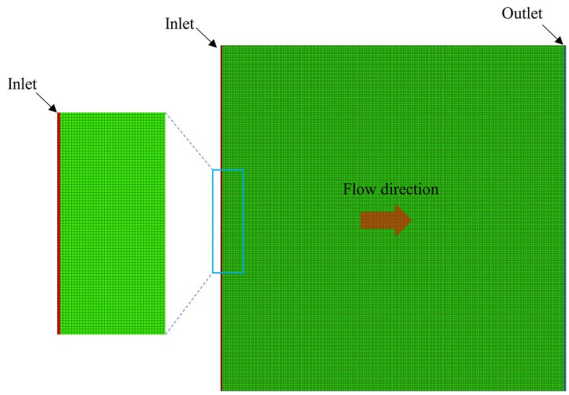

Fig. 18 Model calibration

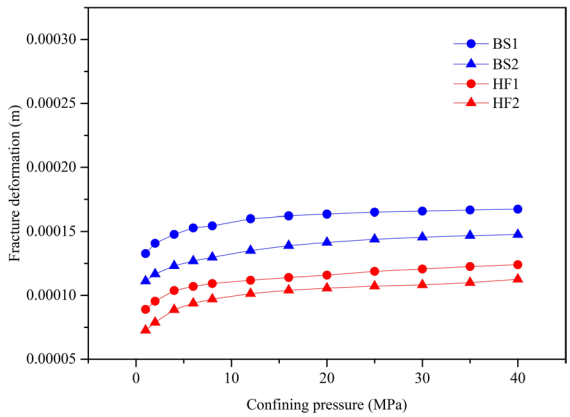

Fig. 19 Fracture deformation at each confining pressure

flow process and can be solved with the finite volume approach Eq. (22):

$$\nabla\rho\frac{e_g^3}{12\mu}\nabla P=0 \tag{21}$$

$$\sum_{j=1}^{n}\frac{e_g^2A_{Cj}}{12\mu\Delta L_j}P_j-\sum_{j=1}^{n}\frac{e_g^2A_{Cj}}{12\mu\Delta L_j}P_o=0 \tag{22}$$

where e_g is the geometrical aperture, [m]; the subscript o stands for the central element; j represents the element adjacent to the central element; A_C is the connecting area. The inlet pressure (0.2 MPa) and outlet pressure (0.1 MPa), which are included in the flow tests, are imposed to the left and right sides indicated in Fig. 18. The top and bottom are blocked for fluid transportation. Herein, two flow directions are defined: (1) x direction, as shown in Fig. 2, which is consistent with the experimental case; (2) y direction perpendicular to the experimental case. According to the numerically computed flow rate and the imposed boundary pressure at the inlet and outlet, the permeabilities in both directions can be evaluated. The strategy is that when one surface of the fracture embeds into the other, the permeability decreases due to the decrease in the geometrical aperture. In this view, the variation of the permeability in response to the increased normal stress can be numerically reproduced. In comparison with experimentally measured results (Fig. 6), the fracture deformation at each

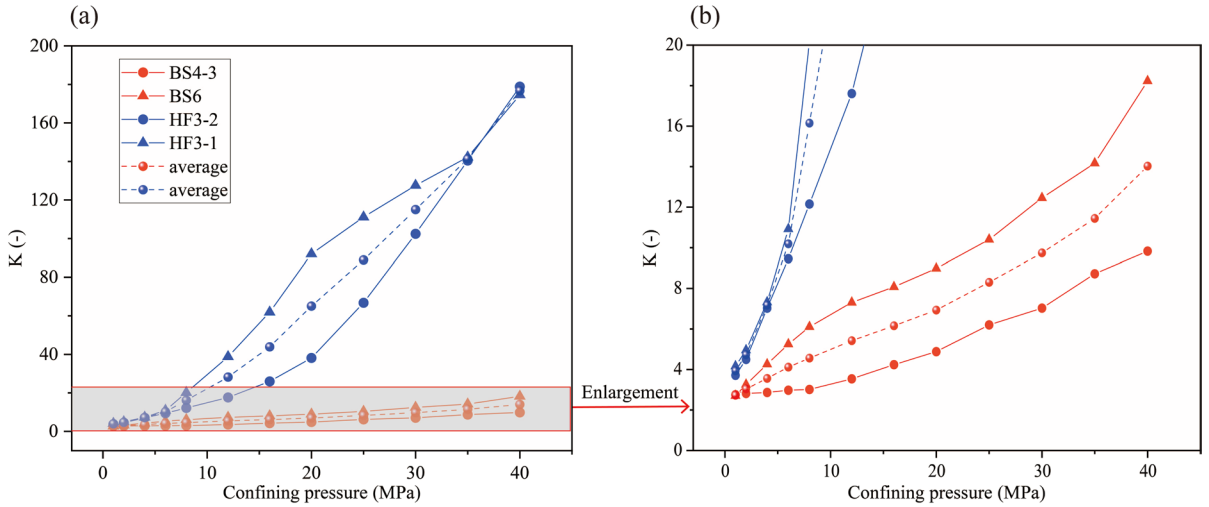

Fig. 20 Comparisons of permeability anisotropy ratios for splitting and hydraulic fractures with the increase of confining pressure from 1 to 40 Mpa: **a** normal view; **b** partial enlarged view

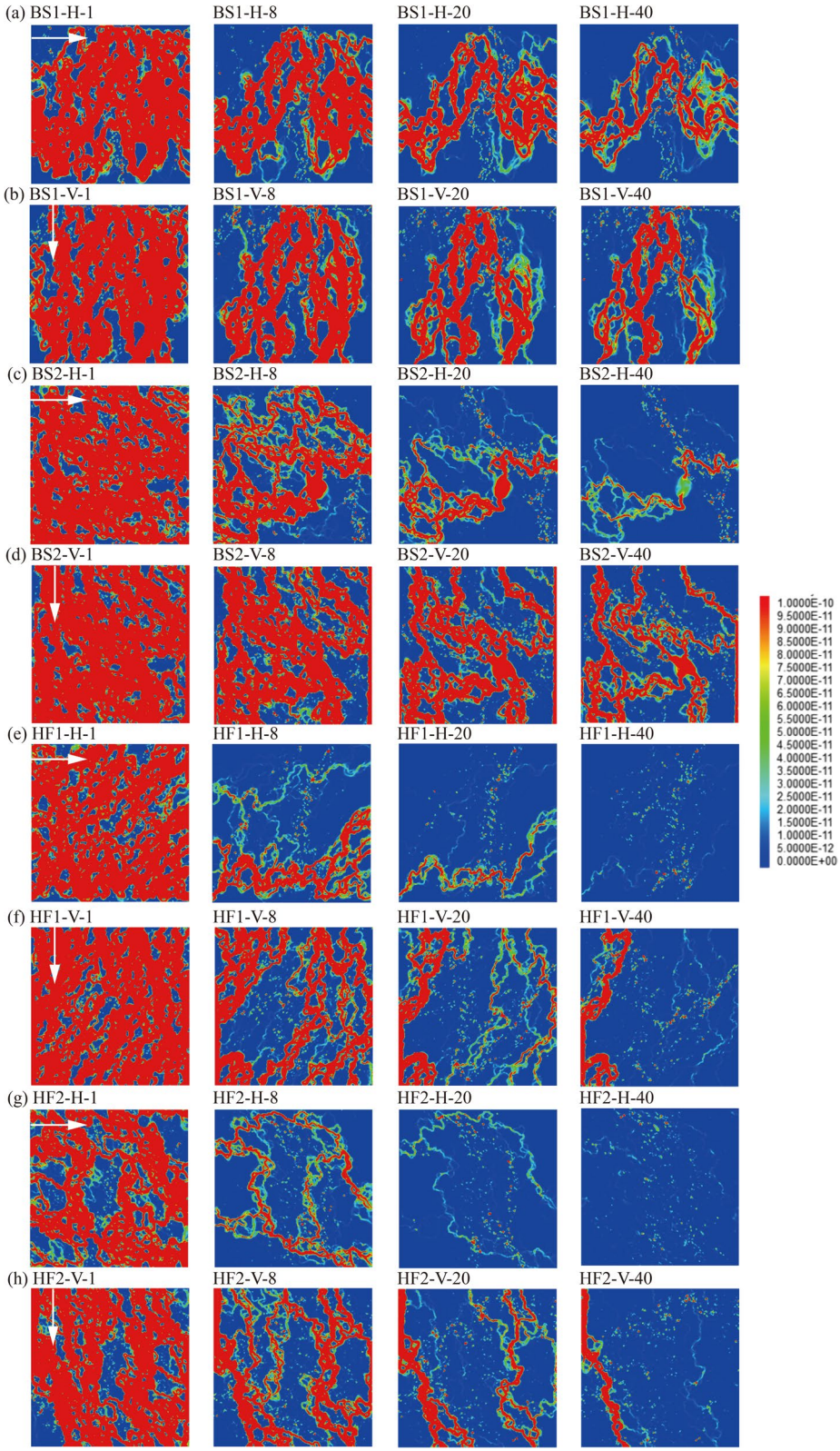
(a) BS1-H-1
BS1-H-8
BS1-H-20
BS1-H-40
(b) BS1-V-1
BS1-V-8
BS1-V-20
BS1-V-40
(c) BS2-H-1
BS2-H-8
BS2-H-20
BS2-H-40
(d) BS2-V-1
BS2-V-8
BS2-V-20
BS2-V-40
(e) HF1-H-1
HF1-H-8
HF1-H-20
HF1-H-40
(f) HF1-V-1
HF1-V-8
HF1-V-20
HF1-V-40
(g) HF2-H-1
HF2-H-8
HF2-H-20
HF2-H-40
(h) HF2-V-1
HF2-V-8
HF2-V-20
HF2-V-40
1.0000E-10
9.5000E-11
9.0000E-11
8.5000E-11
8.0000E-11
7.5000E-11
7.0000E-11
6.5000E-11
6.0000E-11
5.5000E-11
5.0000E-11
4.5000E-11
4.0000E-11
3.5000E-11
3.0000E-11
2.5000E-11
2.0000E-11
1.5000E-11
1.0000E-11
5.0000E-12
0.0000E+00

◂**Fig. 21** Comparisons of flow paths for splitting and hydraulic fractures under different confining pressures: **a**, **b** BS1; **c**, **d** BS2; **e**, **f** HF1; **g**, **h** HF2. 1, 8, 20, 40 represents that confining pressure equals 1 MPa, 8 MPa, 20 MPa, 40 MPa; H stands for horizontal direction; V means vertical direction

loading is obtained for the x flow direction case. After that, the flow direction is changed to y axis and the above process is repeated; then the fracture permeability in y direction for each loading can be determined based on the same fracture deformation from the x flow direction case at the same loading.

4.2 Results

The fracture deformation for splitting and hydraulic fractures are given in the Fig. 19. Fracture deformation is strongly dependent on the confining pressure. At low confining pressures, the incremental rate is large; at high confining pressures, it remains almost constant. On the whole, hydraulic fractures are shown to be less deformable with smaller deformation for a given confining pressure, which is the main reason for that nonlinearity is more difficult to occur in hydraulic fracture.

In this study, the permeability anisotropy ratio K is defined as the ratio of the permeability in x direction to that in y direction. Figure 20 shows variations of the numerically obtained permeability anisotropy ratio for the four fractures in response to the increased confining pressure. It can be found that K is always more than 1 for each case, indicating that the numerically estimated permeability in y direction is smaller than that in x direction. As the confining pressure increases, K gradually increases but exhibit different rates. As a whole, K for hydraulic fractures seem to be more sensitive to the loading, showing that they possess larger K and vary more in response to the increased confining pressure. For the average K, it changes from 2.73 at $\sigma_c = 1$ MPa to 14 at $\sigma_c = 40$ MPa for splitting fractures whereas from 3.94 at $\sigma_c = 1$ MPa to 177 at $\sigma_c = 40$ MPa for hydraulic ones. The difference might be mainly ascribed to rock fracture surface roughness. R_p in the vertical direction ranges from 1.0415 to 1.0436 for splitting fractures and from 1.0376 to 1.0394 for hydraulic ones. For hydraulic fractures, R_p in vertical direction are larger than those in horizontal direction. However, for splitting fractures R_p in vertical direction are close to those in horizontal direction. This is possibly the reason that the permeability anisotropy ratio (K) is much higher in hydraulic fractures compared with that in the spitting fractures.

Variations of the flow paths in the fractures under the confining pressure of 1 MPa, 8 MPa, 20 MPa and 40 MPa for both directions are given in Fig. 21. Since the fracture surface are rather rough (Fig. 2), strong tortuous paths for the flow in both directions exist. As the confining pressure increases, all the flow paths converge to some single paths with small band width which form the bottleneck effect and weaken the flow capacity (Talon et al. 2010). Besides, it is clear that under the same level of the confining pressure, more flow paths are observed in the y flow direction and in the splitting fractures.

5 Conclusions

This study, a number of gas flow tests were performed in a triaxial system on sandstone fracture samples under confining pressure changing from 1 to 40 MPa, primarily for investigating the nonlinear flow characteristics in rock rough fractures. At each level of confining pressure, the gas injection pressure ranges from 0.1 to 2.3 MPa. Fracture geometry, transmissivity, critical Reynolds number, critical pressure gradient, and normalized transmissivity are systematically analyzed. By means of numerical simulation, the permeability anisotropy is also examined in detail. The following conclusions are drawn:

(1) Before gas flow tests, 3D fracture surfaces are first digitally reproduced based on a scanner and then the fracture geometry parameters (R_p, Z_2), aperture distributions are computed for both hydraulic and splitting fractures. The results show that hydraulic fractures possess relatively smoother surfaces with lower R_p, Z_2 and mean aperture.
(2) The transmissivity of splitting fractures is larger than that of hydraulic ones, and the ratio of splitting to hydraulic one varies from 2.51

at $\sigma_c = 1$ MPa to 60.95 at $\sigma_c = 40$ MPa. This is mainly caused by the difference in fracture surface roughness. With a smaller roughness, both walls of a fracture are matched easier and more fracture closure is reached in response to the same loading.

(3) As the confining pressure increases, the critical Reynolds number Re_c decreases and the critical pressure gradient ∇P increases. On the whole, splitting fractures have larger Re_c and lower ∇P, indicating that the occurrence of nonlinear flow in splitting fractures can appear more easily. This is also verified by the average value of Forchheimer coefficient β, 0.00577 for splitting fractures and 0.0041 for hydraulic ones, respectively.

(4) The permeability of sandstone fractures possesses strong anisotropy. This anisotropic effect is dramatically enhanced for a higher loading. On the whole, the permeability anisotropy in hydraulic fracture is more significant, showing that the permeability anisotropy ratios K are larger and more sensitive to the loading.

Author contributions JC: Conceptualization, methodology, supervision. ZC: Data curation, methodology, writing-original draft. XS: conceptualization, software. LZ: Methodology, validation. XL: Validation. LZ: Validation.

Funding The research is financially supported by the Natural Science Foundation of Sichuan Province (No. 2022NSFSC1169), the Scientific Research Foundation of Xihua University (No. Z211014) and the Natural Science Foundation Project of Chongqing (No. cstc2021jcyj-msxmX0929), the National Natural Science Foundation of China (U21A2030; 52204219) and S&T Program of Hebei (No. 22375401D).

Data availability All data that support the findings of this study are available from the corresponding author upon reasonable request.

Declarations

Competing interests The authors declare no competing interests.

Ethical approval The authors confirms that the work described in this paper has not been published elsewhere, nor is it under consideration by another publisher.

Consent to publish Depending on the ownership of the journal and its policies, the authors grant the Publisher an exclusive license to publish this article.

References

Brown GO (2002) Henry Darcy and the making of a law. Water Resour Res 38(7):11-1–11-12. https://doi.org/10.1029/2001wr000727

Brown SR, Kranz RL, Bonner BP (1986) Correlation between the surfaces of natural rock joints. Geophys Res Lett 13(13):1430–1433. https://doi.org/10.1029/GL013i013p01430

Chen YF, Zhou JQ, Hu SH, Hu R, Zhou CB (2015) Evaluation of Forchheimer equation coefficients for non-Da-rcy flow in deformable rough-walled fractures. J Hydrol 529:993–1006. https://doi.org/10.1016/j.jhydrol.2015.09.021

Chen JC, Zhou L, Li HL, Shen ZH, Xia BW (2020) Comparison on hydraulic and mechanical responses to the growing loading between both fractures induced by hydraulic fracturing and Brazilian splitting. Energy Fuels 34(9):10933–10946. https://doi.org/10.1021/acs.energyfuels.0c02233

Dong J, Ju Y (2020) Quantitative characterization of single-phase flow through rough-walled fractures with variable apertures. Geomech Geophys Geo-Energ Geo-Resour 6:42. https://doi.org/10.1007/s40948-020-00166-w

Jang HS, Kang SS, Jang BA (2014) Determination of joint roughness coefficients using roughness parameters. Rock Mech Rock Eng 47(6):2061–2073. https://doi.org/10.1007/s00603-013-0535-z

Javadi M, Sharifzadeh M, Shahriar K (2010) A new geometrical model for non-linear fluid flow through rough fractures. J Hydrol 389(1):18–30. https://doi.org/10.1016/j.jhydrol.2010.05.010

Javadi M, Sharifzadeh M, Shahriar K, Mitani Y (2014) Critical Reynolds number for nonlinear flow through rou-gh-walled fractures: the role of shear processes. Water Resour Res 50(2):1789–1804. https://doi.org/10.1002/2013WR014610

Kulatilake PHSW, Park JY, Balasingam P, Morgan R (2008) Quantification of aperture and relations between aperture, normal stress and fluid flow for natural single rock fractures. Geotech Geol Eng 26(3):269–281. https://doi.org/10.1007/s10706-007-9163-2

Kulatilake PHSW, Park J, Su XP (2020) Fluid flow through natural single-rock fractures: experimental and numerical investigations. Int J Geomech 20(10):04020168. https://doi.org/10.1061/(ASCE)GM.1943-5622.0001790

Li B, Wong RCK, Milnes T (2014) Anisotropy in capillary invasion and fluid flow through induced sandstone and shale fractures. Int J Rock Mech Min Sci 65:129–140. https://doi.org/10.1016/j.ijrmms.2013.10.004

Lomize GM (1951) Flow in fractured rocks. Gosenergoizdat, Moscow

Ma H, Wang J, Feng P, Qian JZ, Tan XH, Luo QK (2022) Effect of high confining pressure on flow behavior and hydraulic aperture considering fractured rock deformation. Geomech Geophys Geo-Energ Geo-Resour 8:155. https://doi.org/10.1007/s40948-022-00471-6

Maerz NH, Franklin JA, Bennett CP (1990) Joint roughness measurement using shadow profilometry. Int J Rock Mech Min Sci Geomech Abstr 27(5):329–343. https://doi.org/10.1016/0148-9062(90)92708-M

McCraw C, Edlmann K, Miocic J, Gilfllan S, Haszeldine RS, McDermott CI (2016) Experimental investigation and hybrid numerical analytical hydraulic mechanical simulation of supercritical CO_2 flowing through a na-tural fracture in caprock. Int J Greenhouse Gas Control 48(1):120–133. https://doi.org/10.1016/j.ijggc.2016.01.002

Méheust Y, Schmittbuhl J (2000) Flow enhancement of a rough fracture. Geophys Res Lett 27:2989–2992. https://doi.org/10.1029/1999gl008464

Méheust Y, Schmittbuhl J (2001) Geometrical heterogeneities and permeability anisotropy of rough fractures. J Geophys Res 106:2089–2102. https://doi.org/10.1029/2000jb900306

Myers NO (1962) Characterization of surface roughness. Wear 5(3):182–189. https://doi.org/10.1016/0043-1648(62)90002-9

Nazridoust K, Ahmadi G, Smith DH (2006) A new friction factor correlation for laminar, single-phase flows through rock fractures. J Hydrol 329(1–2):315–328. https://doi.org/10.1016/j.jhydrol.2006.02.032

Nemoto K, Watanabe N, Hirano N, Tsuchiya N (2009) Direct measurement of contact area and stress dependence of anisotropic flow through rock fracture with heterogeneous aperture distribution. Earth Planet Sci Lett 281(1–2):81–87. https://doi.org/10.1016/j.epsl.2009.02.005

Pang W, Du J, Zhang T, Ehlig-Economides CA (2016) Actual and optimal hydraulic-fracture design in a tight gas reservoir. SPE Prod Oper 31(1):60–68. https://doi.org/10.2118/168613-PA

Qian JZ, Zhan HB, Zhao WD, Sun FG (2005) Experimental study of turbulent unconfined groundwater flow in a single fracture. J Hydrol 311(1):134–142. https://doi.org/10.1016/j.jhydrol.2005.01.013

Ranjith PG, Viete DR (2011) Applicability of the 'cubic law' for non-Darcian fracture flow. J Pet Sci Eng 78(2):321–327. https://doi.org/10.1016/j.petrol.2011.07.015

Rong G, Yang J, Cheng L, Zhou CB (2016) Laboratory investigation of nonlinear flow characteristics in rough f-ractures during shear process. J Hydrol 541:1385–1394. https://doi.org/10.1016/j.jhydrol.2016.08.043

Shen ZH, Zhou L, Li HL, Lu ZH, Cai JC (2020) Experimental and numerical study on the anisotropic and nonlinear gas flow behavior of a single coal fracture under loading. Energy Fuels 34(4):4230–4242. https://doi.org/10.1021/acs.energyfuels.0c00012

Skjetne E, Hansen A, Gudmundsson JS (1999) High-velocity flow in a rough fracture. J Fluid Mech 383:1–28. https://doi.org/10.1017/s0022112098002444

Su XP, Liu JJ, Liu HJ, Zhou L, Li HL, Chen JC (2021) Comparison of shear and tensile fracture permeability in granite under loading-unloading stress conditions. J Porous Media 24(12):93–114. https://doi.org/10.1615/JPorMedia.2021038053

Talon L, Auradou H, Hansen A (2010) Permeability estimates of self-affine fracture faults based on generalizati-on of the bottleneck concept. Water Resour Res 46(7):1–5. https://doi.org/10.1029/2009wr008404

Walsh JB (1981) Effect of pore pressure and confining pressure on fracture permeability. Int J Rock Mech Min Sci Geomech Abstr 18(5):429–435. https://doi.org/10.1016/0148-9062(81)90006-1

Wang CS, Jiang YJ, Liu RC, Wang C, Zhang ZY, Sugimoto S (2020) Experimental study of the nonlinear flow characteristics of fluid in 3D rough-walled fractures during shear process. Rock Mech Rock Eng 53(6):2581–2604. https://doi.org/10.1007/s00603-020-02068-5

Watanabe N, Hirano N, Tsuxhiya N (2008) Determination of aperture structure and fluid flow in a rock fracture by high-resolution numerical modeling on the basis of a flow-through experiment under confining pressure. Water Resour Res 44:W06412. https://doi.org/10.1029/2006WR005411

Witherspoon PA, Wang JSY, Iwai K, Gale JE (1980) Validity of cubic law for fluid flow in a deformable rock fracture. Water Resour Res 16(6):1016–1024. https://doi.org/10.1029/WR016i006p01016

Xie J, Gao MZ, Zhang R, Peng GY, Lu T, Wang F (2020) Experimental investigation on the anisotropic fractal characteristics of the rock fracture surface and its application on the fluid flow description. J Petrol Sci Eng 191:107190. https://doi.org/10.1016/j.petrol.2020.107190

Xiong F, Jiang QH, Ye ZY, Zhang XB (2018) Nonlinear flow behavior through rough-walled rock fractures: the effect of contact area. Comput Geotech 102:179–195. https://doi.org/10.1016/j.compgeo.2018.06.006

Ye ZY, Liu HH, Jiang QH, Liu YZ, Cheng AP (2017) Two-phase flow properties in aperture-based fractures under normal deformation conditions: analytical approach and numerical simulation. J Hydrol 545:72–87. https://doi.org/10.1016/j.jhydrol.2016.12.017

Yeo IW, de Freitas MH, Zimmerman RW (1998) Effect of shear displacement on the aperture and permeability of a rock fracture. Int J Rock Mech Min Sci 35:1051–1070. https://doi.org/10.1016/S0148-9062(98)00165-X

Yin Q, Ma GW, Jing HW, Wang HD, Su HJ, Wang YC, Liu RC (2017) Hydraulic properties of 3D rough-walled fractures during shearing: an experimental study. J Hydrol

555:169–184. https://doi.org/10.1016/j.jhydrol.2017.10.019

Zhang Z, Nemcik J (2012) Friction factor of water flow through rough rock fractures. Rock Mech Rock Eng 46(5):1125–1134. https://doi.org/10.1007/s00603-012-0328-9

Zhou JQ, Hu SH, Fang S, Chen YF, Zhou CB (2015) Nonlinear flow behavior at low Reynolds numbers through rough–walled fractures subjected to normal compressive loading. Int J Rock Mech Min Sci 80:202–218. https://doi.org/10.1016/j.ijrmms.2015.09.027

Zhou JQ, Hu SH, Chen YF, Wang M, Zhou CB (2016) The friction factor in the Forchheimer equation for rock fractures. Rock Mech Rock Eng 49(8):3055–3068. https://doi.org/10.1007/s00603-016-0960-x

Zhu Q, Yin Q, Huang N, Wu JY, Zhang Q, Li T, Yu LY (2022) Assessment of nonlinear flow behaviors through real rough rock fractures during shearing. Geomech Geophys Geo-Energ Geo-Resour 8:171. https://doi.org/10.1007/s40948-022-00489-w

Zimmerman RW, Bodvarsson GS (1996) Hydraulic conductivity of rock fractures. Transp Porous Med 23(1):1–30. https://doi.org/10.1007/bf00145263

Zimmerman RW, Kumar S, Bodvarsson GS (1991) Lubrication theory analysis of the permeability of rough-walled fractures. Int J Rock Mech Min Sci Geomech Abstr 28(4):325–331. https://doi.org/10.1016/0148-9062(91)90597-F

Zimmerman RW, Al-Yaarubi A, Pain CC, Grattoni CA (2004) Non-linear regimes of fluid flow in rock fractures. Int J Rock Mech Min Sci 41:163–169. https://doi.org/10.1016/j.ijrmms.2004.03.036

Zou LC, Jing L, Cvetkovic V (2015) Roughness decomposition and nonlinear fluid flow in a single rock fracture. Int J Rock Mech Min Sci 75:102–118. https://doi.org/10.1016/j.ijrmms.2015.01.016

Zou LC, Jing LR, Cvetkovic V (2017) Shear-enhanced nonlinear flow in rough-walled rock fractures. Int J Rock Mech Min Sci 97:33–45. https://doi.org/10.1016/j.ijrmms.2017.06.001